Miniaturized Single-Photon Level Computational Complex Field Imaging System via Meta-Optics

Yuhao Wang, Qihao Jin, Chongwu Shao, Qiaoshuang Zhang, Judith K. Hohmann, Alban Muslija, Shijian Li, Zhigang Li, Uli Lemmer,* Xuri Yao,* and Qing Zhao**

Compact optical systems are revolutionizing precision measurement with their miniaturized design and functionality. At the forefront of this revolution are metalenses, composed of sub-wavelength nanostructures. They have emerged as novel planar optical elements capable of replacing traditional bulky lenses in various compact optical applications. Meanwhile, single-pixel imaging provides a cost-effective, computation-based method for achieving exceptional imaging quality. In this work, a metalens is integrated with a single-pixel imaging architecture to project high-resolution Hadamard patterns onto microscopic samples, replacing conventional lens-to-detector configurations. The system can simultaneously retrieve high-quality amplitude and phase maps of micro targets, even under single-photon-level illumination conditions (1.7 photons/pixel/s). This breakthrough is ideal for biological samples, particularly in live cell imaging, where minimizing light exposure is critical to avoid photobleaching and phototoxicity. By delivering a cost-effective, compact, and high-performance solution, this system sets a new era for precision imaging in science and industry.

1. Introduction

Microscopic imaging techniques play a significant role in a wide range of scientific research areas.[1–4] However, conventional microscopic imaging systems, such as fluorescence microscopy,[5–8] confocal microscopy,[9] and complex-field microscopy,[10] are typically constructed with heavy and bulky optical components to achieve high imaging performance. Consequently, there is a rapidly growing demand for lightweight, compact, and integrated microscopic systems suitable for small-scale applications.

In recent years, metalenses have emerged as novel, compact planar optical elements that consist of artificial dielectric sub-wavelength nanofins.[11–13] Those nanostructures are carefully designed to manipulate light at the nanoscale, enabling precise control over amplitudes, phases, and polarizations of transmitted or reflected light by varying the dielectric material, as well as the size, shape, rotation angle, and spatial arrangement of the nanofins.[14–18] Because of their compactness and suitability to be integrated into existing optical systems, metalenses are more and more often applied as substitutes for traditional bulky optical components in many different kinds of applications, such as achromatic focal lenses,[19,20] microscopic

Y. Wang, C. Shao, X. Yao, Q. Zhao
Center for Quantum Technology Research and Key Laboratory of
Advanced Optoelectronic Quantum Architecture and Measurements
School of Physics
Beijing Institute of Technology
100081 Beijing, China
E-mail: yaoxuri@bit.edu.cn; qzhaoyuping@bit.edu.cn

Y. Wang, C. Shao, X. Yao, Q. Zhao
Kunming Institute of Physics
650221 Kunming, China

Q. Jin, Q. Zhang, U. Lemmer
Light Technology Institute
Karlsruhe Institute of Technology (KIT)
76131 Karlsruhe, Germany
E-mail: qihao.jin@kit.edu; ulrich.lemmer@kit.edu

J. K. Hohmann, A. Muslija
Karlsruhe Nano Micro Facility (KNMFi)
Karlsruhe Institute of Technology (KIT)
76131 Karlsruhe, Germany

J. K. Hohmann, A. Muslija, U. Lemmer
Institute of Microstructure Technology (IMT)
Karlsruhe Institute of Technology (KIT)
76131 Karlsruhe, Germany

S. Li
School of Integrated Circuits and Electronics
Beijing Institute of Technology
100081 Beijing, China

Z. Li
Institute of Microelectronics of the Chinese Academy of Sciences
100029 Beijing, China

ADVANCED
SCIENCE NEWS

www.advancedsciencenews.com

ADVANCED
OPTICAL
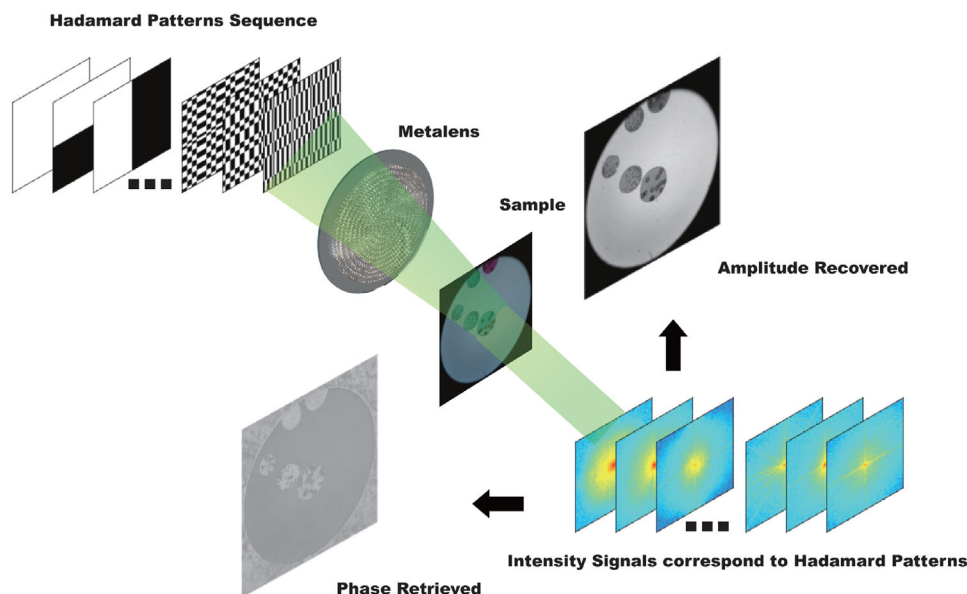**MATERIALS**

www.advopticalmat.de

Figure 1. Schematic of Meta-Single-Pixel Imaging. Hadamard mask patterns, generated by DMD, are projected onto the sample via the metalens. The resulting intensity signals are captured by a detector. Using an effective single-pixel imaging algorithm, both the amplitude and phase maps of the sample are reconstructed from the captured signals.

imaging,[21] holographic displays,[22] orbital angular momentum (OAM) beam generators,[23] modulation components,[24], encryption,[25] and spectrometers.[26] Because of the general Snell's law,[27] metalenses can produce significantly smaller focal spots compared to conventional lenses. Such properties make metalenses particularly suitable for projecting mask patterns with high resolution on tiny biological samples.

Unlike conventional imaging methods that rely on multi-pixel array sensors, single-pixel imaging (SPI) system utilizes a single-point detector and operates by employing a digital micromirror device (DMD) or a spatial light modulator (SLM) to either illuminate an object with encoded structured light patterns or modulate the light carrying the spatial information,[28,29] offering several advantages, including reduced cost, enhanced efficiency, and most notably, simplified hardware requirements. SPI has also emerged as an innovative computational imaging technique rooted in compressive sensing (CS) theory,[30] allowing it to overcome the limitations of traditional imaging systems, which makes it highly adaptable for advanced applications like X-ray imaging,[31] light detection and ranging (LiDAR),[32] and fluorescence microscopy.[33] One of the most notable strengths of SPI is its high throughput,[34] which enables effective performance in extremely low-light conditions, even down to the single-photon level.[35,36] In contrast, achieving such sensitivity is highly challenging for traditional imaging systems based on array sensors. For instance, electron multiplying charge-coupled device (EMCCD) cameras typically suffer from higher readout noise, limited quantum efficiency, and the need for a complex cooling system to suppress thermal noise under low illumination conditions. Additionally, SPI inherently possesses the property of dimensional reduction,[37] efficiently transforming high-dimensional spatial information into low-dimensional intensity measurements through structured light patterns. This makes

SPI capable of not only retrieving high-quality amplitude images but also reconstructing phase maps.[38–40]

In this work, we propose a compact meta-single-pixel microscopic imaging system that synergistically integrates a metalens with active illumination SPI techniques. Unlike those metasurface-based SPI implementations, which primarily focus on optical mask modulation or encryption,[24,25], our system employs a metalens to significantly reduce the overall footprint (approximately 4 cm from DMD to PMT) while enabling high-resolution structured projection. The system demonstrates robustness under low-light conditions, resolving feature sizes as small as 12 μm with a structural similarity index (SSIM) of 0.7993 and peak signal-to-noise ratio (PSNR) of 18.05 dB, and successfully reconstructing 17.5 μm features even at single-photon level illumination (1.7 photon/pixel/s). Beyond capturing high-quality amplitude images of biological samples, it also retrieves phase maps, enabling complex-field imaging from a single-pixel detector. This work presents a compact, sensitive, and scalable imaging platform well-suited for applications such as live cell imaging under low-light conditions and portable diagnostics in the future.

2. Results

2.1. Overview of the Meta-Single-Pixel Microscopic Imaging System

The working principle of the system is demonstrated in **Figure 1**. Generally, the process of SPI can be simply expressed as:

$$g = Mo, \tag{1}$$

e01310 (2 of 10)

ADVANCED
SCIENCE NEWS

www.advancedsciencenews.com

ADVANCED
OPTICAL
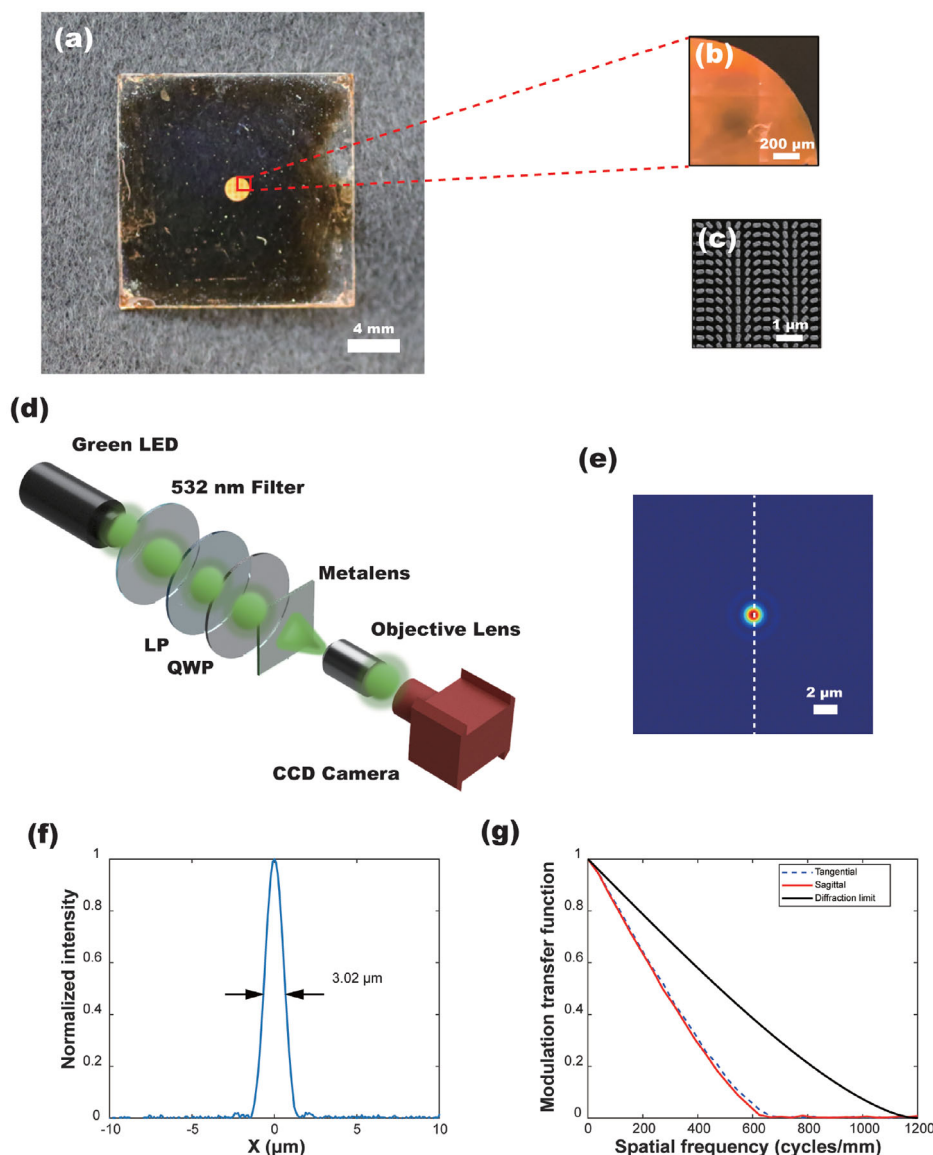**MATERIALS**

www.advopticalmat.de

Figure 2. Characterization of the Fabricated Metalens. a) Optical image of the fabricated metalens with an NA of 0.316 and a diameter of 2 mm. b) Magnified optical photograph showing a detailed view of the fabricated metalens. c) SEM image of the fabricated metalens with a scale bar of 1 µm. d) Schematic of the optical setup used for characterizing the metalens. e) Measured focal plane intensity distribution of the fabricated metalens. f) Vertical cuts across the measured focal spot in (e). g) The calculated tangential and sagittal MTFs of the metalens.

where g denotes the measured value, M represents the measurement matrix—each row of which is formed by reshaping a corresponding mask pattern into a row vector, and the number of columns corresponds to the total number of measurements. And o is the imaging target which is reshaped into a column vector. According to the measured value g as well as the designed mask M, the image of the object o can be calculated. In order to encode spatial information, the total number of 8192 Hadamard mask patterns generated by the DMD are projected onto a micro target sample via a metalens. The metalens efficiently focuses the structured illumination onto the sample, ensuring high-resolution Hadamard mask patterns projection while maintaining the compactness of the total system. The corresponding modulated components of the Hadamard intensity spectrum encoded with the

spatial information of the target are then captured by a single-pixel detector at the Fourier plane. By employing an efficient single-pixel imaging reconstruction algorithm, both the amplitude and phase of the target image are simultaneously retrieved. This reconstruction process leverages the orthogonality of the Hadamard basis to optimize signal acquisition, enabling high-fidelity image recovery even at reduced sampling rates.

2.2. Characterization of Metalens

For a proof of concept demonstration, a relatively large metalens, which is shown in **Figure 2a**, with a diameter of 2 mm and a focal length of 3 mm was fabricated for this meta-single-pixel

e01310 (3 of 10)

**ADVANCED
SCIENCE NEWS**

www.advancedsciencenews.com

**ADVANCED
OPTICAL
MATERIALS**

www.advopticalmat.de

microscopic imaging system, and a magnified view of a portion of this metalens is provided in Figure 2b. The numerical aperture (NA), which is 0.316, can be calculated using the following equation:

$$NA = n_0 sin\theta = n_0 sin(arctan(\frac{r}{f})), \qquad (2)$$

where n_0 denotes the refractive index of air, θ presents the half-maximum angle of light acceptance, r is the radius of metalens, and f is the focal length of metalens. The microstructure quality of the metalens was further investigated using scanning electron microscopy (SEM), as demonstrated in Figure 2c, where a scale bar of 1 µm is provided for reference.

To characterize the imaging performance of the fabricated metalens, an in-house developed experimental setup was utilized, as demonstrated in Figure 2d. A green light-emitting diode (LED) with a central wavelength of 532 nm, served as the illumination source. In order to minimize the influence of chromatic aberrations, a 532 nm line filter (Thorlabs, FBW5532-10) was set behind the light source. Since the metalens was designed based on the Pancharatnam-Berry (PB) phase principle, it is polarization-sensitive (Details in Supporting Information, S1). To ensure that only left-handed circular polarized (LCP) light reached the metalens, a linear polarizer (LBTEK, FLP25-VIS-M) followed by a quarter-wave plate (QWP) (LBTEK, MQWP20-532BM) was introduced to the optical path, thereby eliminating contributions from unwanted polarization states. The focal spot intensity distribution at 532 nm, captured by using a 40 × magnification Olympus objective lens and charge-coupled device (CCD) camera (IMPERX, B1620), is presented in Figure 2e. The corresponding full width at half maximum (FWHM) of the focal spot was measured to be 3.02 µm, as shown in Figure 2f. In addition, the modulation transfer function (MTF), calculated from the experimentally measured point spread function (PSF),[41,42] is shown for both tangential and sagittal planes in Figure 2g. The approaching curves of MTF on both tangential and sagittal planes indicate good symmetry of the metalens. The focal efficiency of the metalens at 532 nm was measured to be approximately 37.38%, using the optical setup detailed in Supporting Information, S2.

2.3. Meta-Single-Pixel Microscopic Imaging System

Figure 3 illustrates the imaging experiment setup, where the distance between the DMD and the PMT is approximately 4 cm, significantly smaller than the systems developed by state of art.[43–48] An LED (KM-SPP505-W) with a central wavelength of 532 nm served as the light source, providing stable and uniform illumination. To reduce the system's overall size and components count, a linear polarizer (LBTEK, FLP25-VIS-M) was placed immediately after the LED. Linearly polarized light can be considered a superposition of LCP and right-handed circularly polarized (RCP) components. Although only the LCP component contributes effectively to the system's performance, the undesired RCP component does not introduce significant artifacts. This robustness is attributed to the system's use of a Hadamard differential modulation strategy, which effectively cancels out the divergence effects introduced by RCP light. Further details on this suppres-
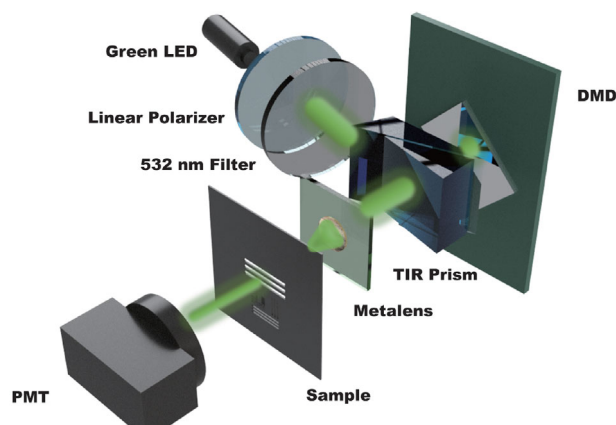

Figure 3. Schematic of the imaging setup. The schematic illustrates the microscopic meta-single-pixel imaging system with a test sample.

sion mechanism are provided in the next section. Furthermore, a 532 nm line filter (Thorlabs, FBW5532-10) was placed following the polarizer to minimize the impact of chromatic aberrations, enhancing the performance of the whole system. Moreover, to reduce the optical footprint and enable compact integration, a self-balsaming total internal reflection (TIR) prism was introduced. This prism serves two key purposes: it minimizes the physical space otherwise occupied by mechanical mounts, and it compensates for the 12° tilt of the DMD's micromirrors. Additional details about the optical path correction can be found in Supporting Information, S3. The DMD (Texas Instruments, DLP9500) was positioned in the optical path to generate structured illumination patterns by modulating the incident beam with Hadamard masks (pixel size of 128 × 128, where every 2 × 2 is merged into a single super-pixel). Behind the TIR prism, the fabricated metalens played a central role in this system. The encoded mask patterns were projected onto the samples through the metalens, forming high-resolution, structured, and tightly focused illumination at the sample plane. As for the samples themselves, they were mounted on a motorized stage capable of fine positional adjustment in three dimensions. At the final stage of the system, a PMT (Hamamatsu, H10682-210) was used, which was placed at the Fourier plane to record the corresponding modulated intensity spectrum.

2.4. Hadamard Differential Modulation

Hadamard matrices are composed of +1 and –1, with the property that any two distinct rows or columns are mutually orthogonal.[49] These matrices can be converted into a complementary pair of binary masks suitable for using in SPI via a differential transformation.[50–53] Specifically, each Hadamard fundamental mode I^i is transformed into two complementary masks I^i_+ ($I^i_+ = \frac{1}{2}(I^i + 1)$) and I^i_- ($I^i_- = 1 - I^i_+$) consisting 0 and 1. And the corresponding measurements of the SPI detector can be demonstrated as g^i_+ and g^i_-. When m Hadamard masks are projected onto the object, the corresponding measurements g^i ($i = 1,...,m$) are collected and arranged into a column vector g of m rows. Hence, the corresponding measurements can be obtained by performing

**ADVANCED
SCIENCE NEWS**

www.advancedsciencenews.com

**ADVANCED
OPTICAL
MATERIALS**

www.advopticalmat.de

differential processing on sequential measurements of a mask pair, which can be mathematically expressed as:

$$g^i = g^i_+ - g^i_- = <I^i_+, o> - <I^i_-, o>, \tag{3}$$

where o represents the object.

Linear polarized light can be treated as a superposition of LCP and RCP light. When using linear polarized light as the incident light field, the process can be demonstrated as the following equation:

$$g^i = <I^i_{+,LCP} + I^i_{+,RCP}, o> - <I^i_{-,LCP} + I^i_{-,RCP}, o>. \tag{4}$$

Since the PB-phase-designed metalens focuses only on LCP light while RCP light diverges, the RCP component forms a non-focused background, effectively behaving like a spatially uniform speckle or a direct current (DC) offset. Hence, Equation (4) could be further demonstrated as:

$$g^i = (<I^i_{+,LCP}, o> + \alpha I^i_{+,RCP}) - (<I^i_{-,LCP}, o> + \alpha I^i_{-,RCP}), \tag{5}$$

where α is the transmittance of object. Since the RCP terms contribute only a constant background, denoted as C, Equation (5) can be finally rewritten as:

$$g^i = (<I^i_{+,LCP}, o> + C) - (<I^i_{-,LCP}, o> + C)$$

$$= <I^i_{+,LCP}, o> - <I^i_{-,LCP}, o>. \tag{6}$$

Above all, when a linear polarizer is incorporated into the system, the diverging light field induced by RCP light is effectively suppressed due to the intrinsic properties of the Hadamard differential modulation employed in the SPI system, ensuring accurate image reconstruction. The comparison of experimental results can be found in the Supporting Information, S4.

2.5. Imaging Results of Amplitude Reconstruction

A series of actual experiments was conducted to evaluate the performance and imaging capability of the compact meta-single-pixel imaging system. Two micro-scale targets were selected for validation: a standard high-resolution transparent negative test target (Thorlabs NBS1963A) and polymethyl methacrylate (PMMA) micro balls with a diameter of 30 μm. Ground-truth images of these targets were acquired using a CCD camera paired with a 5× magnification objective lens (SanWenKeJiao, PL5), as detailed in Supporting Information, S5.

The sampling rate (SR) used in the experiments is defined as:

$$SR = \frac{N}{n_H}, \tag{7}$$

where N represents the number of measurements and n_H denotes the total number of pixels in the Hadamard mask. The single-pixel imaging algorithm was then applied to reconstruct the target's intensity distribution using its measured signal sequence. A detailed description of the reconstruction algorithm is provided in Supporting Information, S6.

Under low-illumination conditions (approximately 37.2k photons per second, recorded by photon counter (Counter 224, Beijing Zhongke Xinji Semiconductor Co., Ltd.)), reconstructed images at different sampling rates (10%, 30%, 50%, 80%, and 100%) are presented in **Figure** 4(a2–a6) and (b2–b6). The group 81 patterns on the test target, corresponding to 81 line pairs per millimeter (lp/mm) or approximately 12 μm in spatial dimension, were reconstructed effectively. To assess the reconstruction accuracy, the intensity profiles along the cross-section of both the directly captured image from the CCD camera and the reconstructed image obtained through the meta-single-pixel imaging system were analyzed as shown in Figure 4c. The comparison demonstrates the ability of the system to faithfully recover fine structural details, with the reconstructed intensity profile closely matching the ground truth. To further evaluate imaging performance, SSIM and PSNR (definitions provided in Supporting Information, S7) were calculated. Simulation results (Supporting Information, S8) indicate that in the low sampling rate range (0–50%), SSIM and PSNR increase rapidly with the number of measurements. However, in the high sampling rate range (80–100%), the SSIM and PSNR decline slightly due to cumulative noise effects. The experimental results, shown in Figure 4d,e, align well with the simulations. To strike a balance among image quality, noise accumulation effect, and computational time (detailed in Supporting Information, S9), a sampling rate of 80% was chosen as optimal. And the noise immunity discussion of the reconstruction method can be found in Supporting Information, S10. At 80% sampling rate, the system effectively reconstructed the group 81 patterns with sharp contours and uniform transmission in the center of the micro balls. The SSIM and PSNR values were 0.7993 and 18.05 dB for group 81 patterns, 0.7903 and 18.78 dB for micro balls, respectively.

Moreover, the proposed meta-single-pixel microscopic imaging system demonstrates a remarkable theoretical and practical capability for image reconstruction even under single-photon level illumination conditions. In the following ultra-low illumination experiments, the average photons were approximately 30k per second and 7k per second, respectively. As shown in Figure 4(f1,f2), after applying FFDNet for noise reduction,[54] the resolution target group 57 (approximately 17.5 μm) was effectively reconstructed at photon flux levels of 7.3 photons/pixel/s and 1.7 photons/pixel/s, with the latter firmly within the single-photon regime. Such extremely low illumination conditions are significant challenges for conventional systems. The resolution discussion of the system can be found in Supporting Information, S11. The successful image reconstruction under these conditions highlights the exceptional sensitivity and photon efficiency of the meta-single-pixel microscopic imaging system, further demonstrating its potential for advanced applications where minimizing light exposure is critical.

2.6. Imaging Results of Phase Retrieve

Additional experiments were performed to assess its imaging capabilities on three kinds of biological samples (motor nerve cells, lily ovary cells, and equisetum spore cells) under low-illumination conditions (approximately 34.5k photons per second on average). **Figure** 5(a1,b1,c1) present direct images of these

ADVANCED
SCIENCE NEWS
www.advancedsciencenews.com
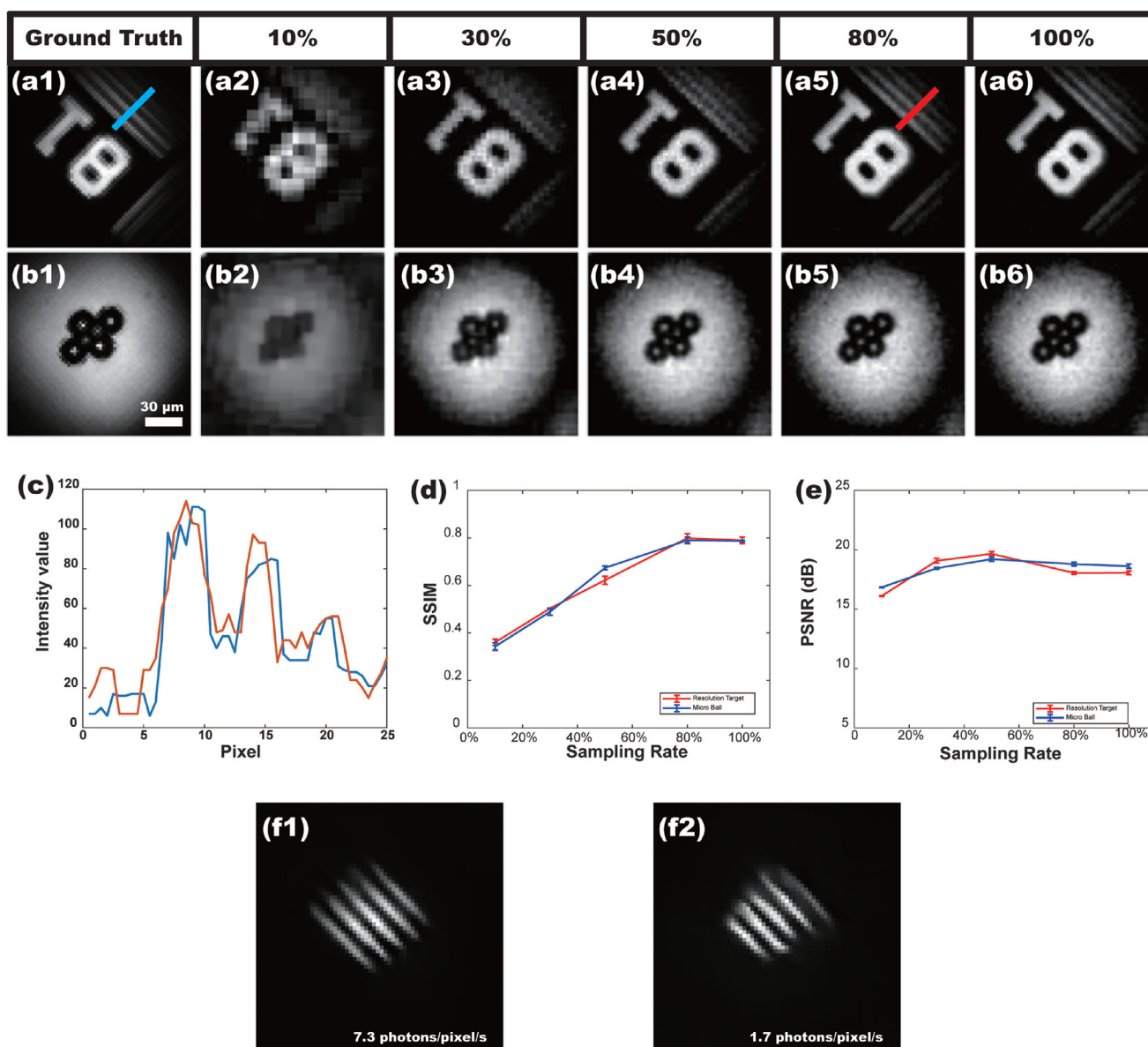
ADVANCED
OPTICAL
MATERIALS
www.advopticalmat.de

Figure 4. Quantitative Amplitude Images of the micro-samples. (a1) Direct image of the resolution target captured by the CCD camera. (a2)–(a6) Reconstructed images of the resolution target at different sampling rates. (b1) Direct image of the micro balls captured by the CCD camera. (b2)–(b6) Reconstructed images of the micro balls at different sampling rates. (c) Intensity profiles of the cross-sectional blue and red lines shown in (a1) and (a5). (d) The variation trend of SSIM as the sampling rate increases. (e) The variation trend of PSNR as the sampling rate increases. (f1) and (f2) Reconstructed images of resolution target at 7.3 photons/pixel/s and 1.7 photons/pixel/s.

samples captured using a microscope with 5× magnification, serving as reference images. The corresponding reconstructed amplitude images obtained with the meta-single-pixel imaging system at 80% sampling rate are shown in Figure 5(a2,b2,c2). The calculated SSIM values for motor nerve cells, lily ovary cells, and equisetum spore cells were 0.7458, 0.5764, and 0.6998, respectively. The PSNRs were 22.04, 16.02, as well as 16.17 dB. The experimental results highlight the versatility of the proposed imaging system, which effectively resolved fine structural details such as branching extensions in motor nerve cells, distinguished individual lily ovary cells with sharply defined walls and visible nuclei, and achieved high-fidelity imaging of equisetum spore cells by clearly delineating external contours, internal features, and adjacent cell walls. Furthermore, retrieved 2D phase maps for these samples, as displayed in Figure 5(a3,b3,c3), highlight the capability of the system to capture complex-field information beyond traditional amplitude imaging. Detailed information on the phase recovery algorithm process is demonstrated in Supporting Information, S12. These findings validate the potential of the meta-single-pixel imaging system as a powerful tool for biological imaging, offering reconstruction capabilities with both amplitude and phase information.
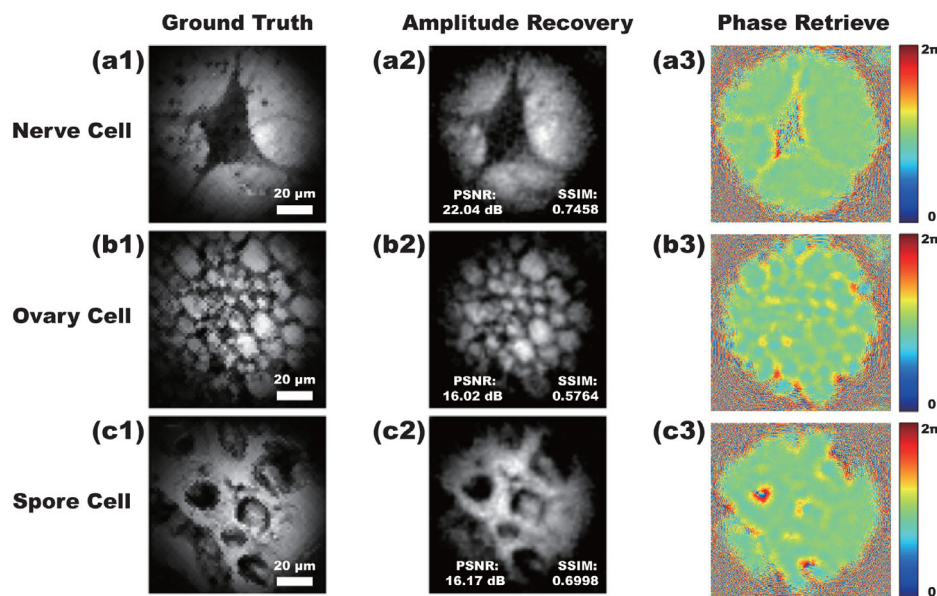
Figure 5. Complex field imaging results of micro samples. (a1), (b1), and (c1) Direct images of micro samples captured by the CCD camera. (a2), (b2), and (c2) Reconstructed amplitude images of the micro samples with 80% sampling rate. (a3), (b3), and (c3) Retrieved 2D phase maps corresponding to each micro sample.
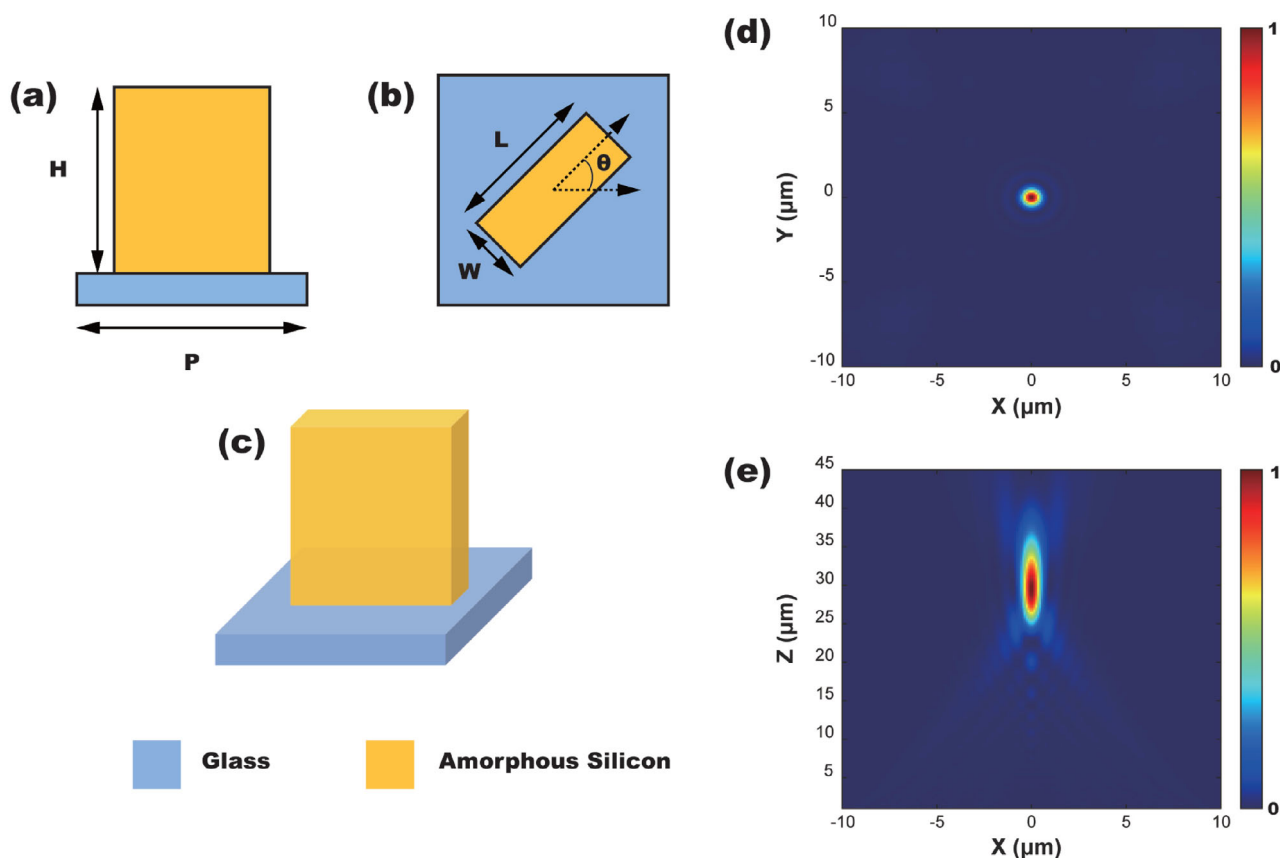

Figure 6. Nanostructure and Simulation Results of Metalens. a) Front view and b) top view of nanostructure of metalens ($H = 300$ nm, $P = 370$ nm, $W = 100$ nm, and $L = 250$ nm). c) Spatial arrangement of the nanostructure. d) Simulated focal intensity distribution of the metalens with a NA of 0.316 at a wavelength of 532 nm on the X-Y plane. e) Simulated longitudinal intensity distribution of the light field cross-section on the X-Z plane at the working wavelength.

**ADVANCED
SCIENCE NEWS**

www.advancedsciencenews.com

**ADVANCED
OPTICAL
MATERIALS**

www.advopticalmat.de

3. Conclusion

In this work, we developed a compact meta-single-pixel imaging system by combining the strengths of metalenses and single-pixel imaging techniques, with a particular emphasis on minimizing the overall system scale. Our approach employs a metalens to project high-resolution Hadamard mask patterns onto micro-samples, replacing the conventional lens-to-detector light collection architecture with a programmable spatial light modulation strategy. Experimental results demonstrate the system's capability to reconstruct both amplitude and phase maps, even under single-photon level illumination conditions, highlighting its exceptional sensitivity and photon efficiency. By enhancing imaging functionality in a compact form, this work paves the way for significant contributions to fields such as live-cell imaging, developmental biology. The integration of meta-optics with computational imaging not only expands the applicability of single-pixel techniques but also sets a foundation for the next generation of high-performance, miniature optical imaging systems, particularly in resource-limited or space-constrained environments.

4. Experimental Section

Phase Design of Metalens: Based on Fermat's principle, the phase $\phi(x, y)$ distribution profile of a typical metalens is expressed as the following equation:[55]

$$\phi(x, y) = \frac{2\pi}{\lambda}(f - \sqrt{x^2 + y^2 + f^2}), \qquad (8)$$

where f is the focal length of the metalens, x and y are Cartesian coordinates location of each nanofin, and λ is the incident wavelength. The relationship between the phase ϕ and the rotation angle θ of each nanofin is given by $\phi = 2\theta$.

Numerical simulations were performed by using a commercial finite-difference-time-domain (FDTD) software package (Lumerical Inc., Vancouver). The focal length of the metalens is inherently wavelength-dependent. Therefore, to eliminate chromatic aberration and ensure accuracy in simulations,[56] a monochromatic incident wavelength λ of 532 nm (widely used as an excitation light source in fluorescence imaging) was used. Generally, metalens materials are typically chosen for their low absorption and loss in the visible range, such as TiO_2 and Si_3N_4. This study employs amorphous silicon (a-Si) as the dielectric material for the nanofins. Although a-Si exhibits relatively higher absorption at 532 nm, its high refractive index of 4.43 enables efficient phase modulation, which is
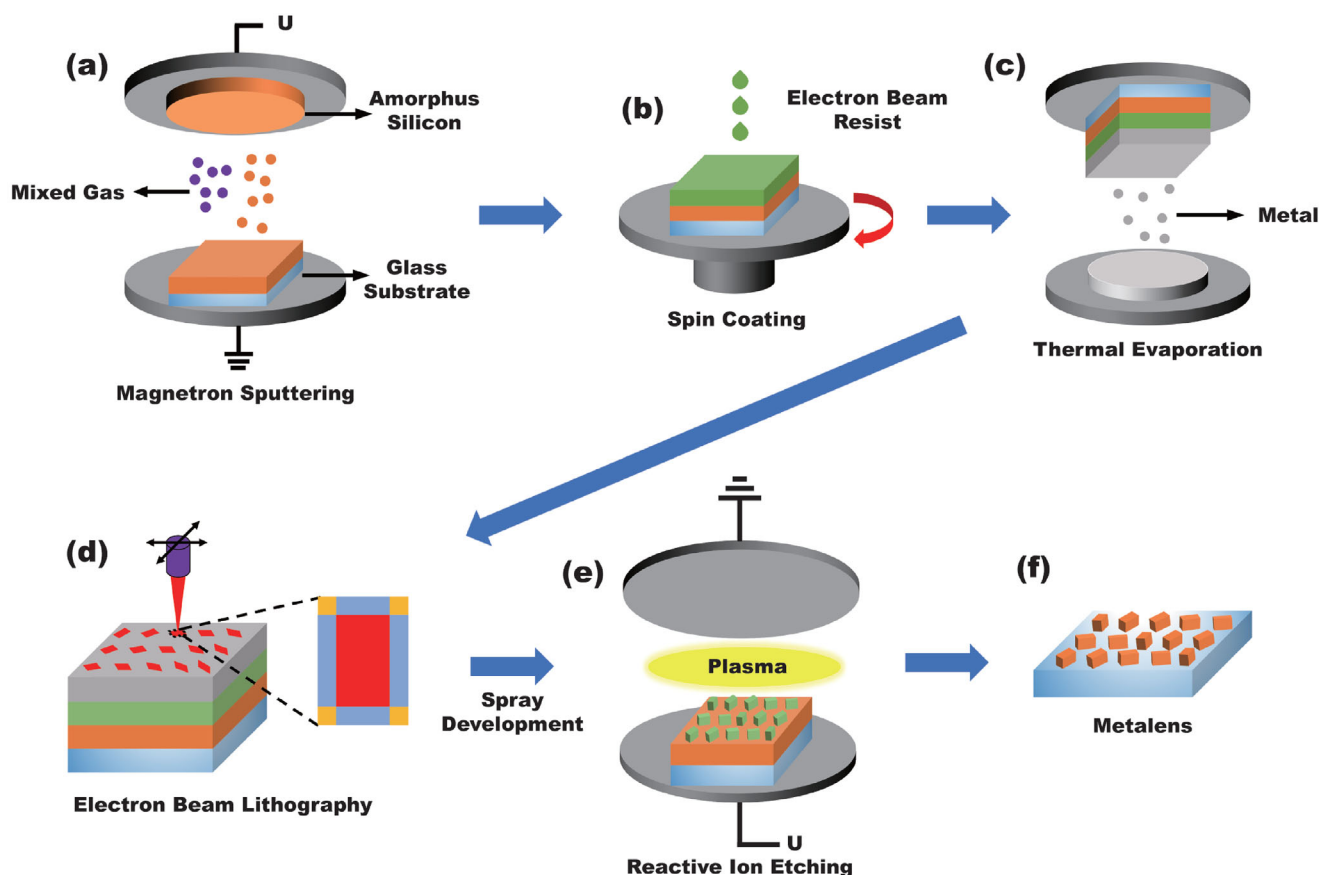

Figure 7. Fabrication process of metalens. a) Amorphous silicon was deposited onto a glass substrate by using magnetron sputtering. b) A negative electron beam resist was spin-coated onto the deposited wafer. c) A thin metallic layer was deposited on the wafer by thermal evaporation. d) Electron beam exposure was performed to generate the nanostructure. e) After spray development, RIE was utilized to precisely transfer the patterned nanostructures from the resist. f) The fabricated metalens.

**ADVANCED
SCIENCE NEWS**

www.advancedsciencenews.com

**ADVANCED
OPTICAL
MATERIALS**

www.advopticalmat.de

critical for metalens performance. Furthermore, the high-throughput property of the SPI system effectively compensates for the associated losses. The measured optical constants of the material can be found in Figure S9, Supporting Information, S13. The substrate material was chosen as fused silica, which has a refractive index of 1.46 at the same wavelength, providing a high refractive index contrast for proper phase modulation. The nanofins were designed as cuboidal structures with a fixed height (H) of 300 nm, arranged on the substrate in a periodic square lattice with a lattice constant (P) of 370 nm, as shown in **Figure 6**a. The geometric dimensions of nanofins were carefully optimized with a length (L) of 250 nm and a width (W) of 100 nm, as shown in Figure 6b, to achieve the required phase shift. Theoretically, taking the fill factor, thickness, and the absorption coefficient, the calculated transmittance is around 40.43%. To balance computational cost and memory limitations, the simulated metalens was designed with a reduced diameter and focal length compared to the real-world implementation. Specifically, the diameter was set to 20 μm and the focal length to 30 μm. However, to ensure that the optical performance of the simulation accurately reflects the real system, the numerical aperture (NA) of the simulated metalens was kept identical to that of the actual design, maintaining a value of approximately 0.316.

Fabrication Process of Metalens: **Figure 7** illustrates the fabrication process of the metalens. First, a 300 nm-thick a-Si layer was deposited onto a fused silica substrate using a magnetron sputtering system. During the deposition process, the chamber was evacuated to a high vacuum to minimize contamination, and then mixed gas (Argon and Nitrogen) was applied as a functional medium. Then, patterning of the metalens structure was performed using electron beam lithography (EBL), followed by a dry etching process to transfer the designed nanostructures onto the amorphous silicon layer. In the EBL process, a negative electron beam resist was spin-coated onto the substrate at a controlled speed to achieve a uniform and precise resist thickness. To ensure optimal electron beam interaction, a thin metallic layer was deposited on top of the resist by thermal evaporation. This metallic layer helped mitigate charging effects during the electron beam exposure, ensuring high-resolution patterning. The patterning was performed using a high-precision 100 kV electron beam lithography system (Raith EBPG 5200Z), which provided the capability of writing nanostructures with feature sizes around 10 nm. The electron beam selectively exposed areas of the resist according to the designed nanofin patterns, following the phase profile distribution of the metalens. To achieve high manufacturing accuracy and ensure sharp edges of nanofins, each nanofin was separated into three parts, as shown in Figure 7d. Each generated nanostructure was divided into three distinct regions: orange (20 nm × 20 nm), light blue (20 nm × 210 nm and 20 nm × 60 nm), and red (60 nm × 210 nm). Development of the resist was carried out using a spray development technique, which ensured uniform and high-fidelity removal of unexposed resist regions. Finally, reactive ion etching (RIE) was employed to transfer nanostructures from the resist onto the underlying a-Si layer. In the RIE process, a carefully controlled plasma environment was created using a mixture of gases to achieve selective etching of the a-Si layer. RIE provided precise anisotropic etching, enabling accurate nanostructures with a high aspect ratio.

Supporting Information

Supporting Information is available from the Wiley Online Library or from the author.

Acknowledgements

Conflict of Interest

The authors declare no conflict of interest.

Data Availability Statement

The data that support the findings of this study are available from the corresponding author upon reasonable request.

Keywords

[1] Y. Park, C. Depeursinge, G. Popescu, *Nat. Photonics* **2018**, *12*, 578.

[2] B. Dai, Z. Jiao, L. Zheng, H. Bachman, Y. Fu, X. Wan, Y. Zhang, Y. Huang, X. Han, C. Zhao, T. J. Huang, S. Zhuang, D. Zhang, *Light: Sci. Appl.* **2019**, *8*, 75.

[3] Y. Xue, I. G. Davison, D. A. Boas, L. Tian, *Sci. Adv.* **2020**, *6*, eabb7508.

[4] K. C. Lee, K. Lee, J. Jung, S. H. Lee, D. Kim, S. A. Lee, *ACS Photonics* **2021**, *8*, 1307.

[5] J. W. Lichtman, J.-A. Conchello, *Nat. Methods* **2005**, *2*, 910.

[6] W. Li, Z. Tong, K. Xiao, Z. Liu, Q. Gao, J. Sun, S. Liu, S. Han, Z. Wang, *Optica* **2019**, *6*, 1515.

[7] Y. Luo, C. H. Chu, S. Vyas, H. Y. Kuo, Y. H. Chia, M. K. Chen, X. Shi, T. Tanaka, H. Misawa, Y.-Y. Huang, D. P. Tsai, *Nano Lett.* **2021**, *21*, 5133.

[8] M.-J. Sun, Y.-C. Zhang, F.-R. Lin, S. Wang, L.-W. Liu, J.-L. Qu, *APL Photonics* **2024**, *9*.

[9] A. D. Elliott, *Curr. Protoc. Cytom.* **2020**, *92*, e68.

[10] W. Osten, A. Faridian, P. Gao, K. Körner, D. Naik, G. Pedrini, A. K. Singh, M. Takeda, M. Wilke, *Appl. Opt.* **2014**, *53*, G44.

[11] S. M. Kamali, E. Arbabi, A. Arbabi, A. Faraon, *Nanophotonics* **2018**, *7*, 1041.

[12] W. T. Chen, A. Y. Zhu, J. Sisler, Z. Bharwani, F. Capasso, *Nat. Commun.* **2019**, *10*, 355.

[13] E. Engay, D. Huo, R. Malureanu, A.-I. Bunea, A. Lavrinenko, *Nano Lett.* **2021**, *21*, 3820.

[14] Y. Zhou, I. I. Kravchenko, H. Wang, J. R. Nolen, G. Gu, J. Valentine, *Nano Lett.* **2018**, *18*, 7529.

[15] R. Zhao, B. Sain, Q. Wei, C. Tang, X. Li, T. Weiss, L. Huang, Y. Wang, T. Zentgraf, *Light: Sci. Appl.* **2018**, *7*, 95.

[16] Y. Ni, S. Chen, Y. Wang, Q. Tan, S. Xiao, Y. Yang, *Nano Lett.* **2020**, *20*, 6719.

[17] F. Zhao, R. Lu, X. Chen, C. Jin, S. Chen, Z. Shen, C. Zhang, Y. Yang, *Laser Photonics Rev.* **2021**, *15*, 2100097.

[18] C. Zhang, S. Divitt, Q. Fan, W. Zhu, A. Agrawal, Y. Lu, T. Xu, H. J. Lezec, *Light: Sci. Appl.* **2020**, *9*, 55.

[19] F. Balli, M. Sultan, S. K. Lami, J. T. Hastings, *Nat. Commun.* **2020**, *11*, 3892.

**ADVANCED
SCIENCE NEWS**

www.advancedsciencenews.com

**ADVANCED
OPTICAL
MATERIALS**

www.advopticalmat.de

[20] Y. Dong, B. Zheng, H. Li, H. Tang, H. Zhao, Y. Huang, S. An, H. Zhang, *ACS Photonics* **2024**, *11*, 1645.

[21] X. Ye, J. Sun, W. Jiang, R. Yu, C. Chen, X. Xiao, X. Qian, C. Huang, Y. Hu, S. Zhu, T. Li, *Advanced Devices & Instrumentation* **2023**, *4*, 0023.

[22] G. Zheng, H. Mühlenbernd, M. Kenney, G. Li, T. Zentgraf, S. Zhang, *Nat. Nanotechnol.* **2015**, *10*, 308.

[23] G. He, Y. Zheng, C. Zhou, S. Li, Z. Shi, Y. Deng, Z.-K. Zhou, *Light: Sci. Appl.* **2024**, *13*, 98.

[24] J. Yan, Y. Wang, Y. Liu, Q. Wei, X. Zhang, X. Li, L. Huang, *Nanophotonics* **2022**, *11*, 3071.

[25] P. Zheng, Q. Dai, Z. Li, Z. Ye, J. Xiong, H.-C. Liu, G. Zheng, S. Zhang, *Sci. Adv.* **2021**, *7*, eabg0363.

[26] X. Hua, Y. Wang, S. Wang, X. Zou, Y. Zhou, L. Li, F. Yan, X. Cao, S. Xiao, D. P. Tsai, J. Han, Z. Wang, S. Zhu, *Nat. Commun.* **2022**, *13*, 2732.

[27] N. Yu, P. Genevet, M. A. Kats, F. Aieta, J.-P. Tetienne, F. Capasso, Z. Gaburro, *science* **2011**, *334*, 333.

[28] G. M. Gibson, S. D. Johnson, M. J. Padgett, *Opt. Express* **2020**, *28*, 28190.

[29] P. G. Vaz, D. Amaral, L. Requicha Ferreira, M. Morgado, J. Cardoso, *Opt. Express* **2020**, *28*, 11666.

[30] M. F. Duarte, M. A. Davenport, D. Takhar, J. N. Laska, T. Sun, K. F. Kelly, R. G. Baraniuk, *IEEE Signal Process. Mag.* **2008**, *25*, 83.

[31] A.-X. Zhang, Y.-H. He, L.-A. Wu, L.-M. Chen, B.-B. Wang, *Optica* **2018**, *5*, 374.

[32] G. A. Howland, P. B. Dixon, J. C. Howell, *Appl. Opt.* **2011**, *50*, 5917.

[33] V. Studer, J. Bobin, M. Chahid, H. S. Mousavi, E. Candes, M. Dahan, *Proc. Natl. Acad. Sci. USA* **2012**, *109*, E1679.

[34] D. Wu, J. Luo, G. Huang, Y. Feng, X. Feng, R. Zhang, Y. Shen, Z. Li, *Nat. Commun.* **2021**, *12*, 4712.

[35] X.-F. Liu, X.-R. Yao, C. Wang, X.-Y. Guo, G.-J. Zhai, *Opt. Express* **2017**, *25*, 3286.

[36] S. Liu, B. Chen, W. Zou, H. Sha, X. Feng, S. Han, X. Li, X. Yao, J. Zhang, Y. Zhang, *Communications Engineering* **2024**, *3*, 88.

[37] K. Song, Y. Bian, D. Wang, R. Li, K. Wu, H. Liu, C. Qin, J. Hu, L. Xiao, *Laser Photonics Rev.* **2024**, 2401397.

[38] F. Soldevila, V. Durán, P. Clemente, J. Lancis, E. Tajahuerce, *Optica* **2018**, *5*, 164.

[39] M. Li, L. Bian, G. Zheng, A. Maiden, Y. Liu, Y. Li, J. Suo, Q. Dai, J. Zhang, *Opt. Lett.* **2021**, *46*, 1624.

[40] Y.-N. Zhao, L. Wang, H. Li, C. Liu, L. Guan, D.-Z. Cao, H.-C. Liu, S.-H. Zhang, *Opt. Laser Technol.* **2025**, *182*, 112017.

[41] Q. Zhang, M. Schambach, S. Schlisske, Q. Jin, A. Mertens, C. Rainer, G. Hernandez-Sosa, M. Heizmann, U. Lemmer, *Adv. Opt. Mater.* **2022**, *10*, 2200677.

[42] Y. Park, Y. Kim, C. Kim, G.-Y. Lee, H. Choi, T. Choi, Y. Jeong, B. Lee, *Adv. Opt. Mater.* **2025**, *13*, 2402853.

[43] N. Radwell, K. J. Mitchell, G. M. Gibson, M. P. Edgar, R. Bowman, M. J. Padgett, *Optica* **2014**, *1*, 285.

[44] Y. Liu, J. Suo, Y. Zhang, Q. Dai, *Opt. Express* **2018**, *26*, 32451.

[45] M. Yao, J. Cheng, Z. Huang, Z. Zhang, S. Li, J. Peng, J. Zhong, *Opt. Express* **2019**, *27*, 33040.

[46] M. Yao, Z. Cai, X. Qiu, S. Li, J. Peng, J. Zhong, *Opt. Express* **2020**, *28*, 6521.

[47] E. Hahamovich, S. Monin, Y. Hazan, A. Rosenthal, *Nat. Commun.* **2021**, *12*, 4516.

[48] G. Wang, H. Deng, Y. Cai, M. Ma, X. Zhong, X. Gong, *Photonics Research* **2024**, *12*, 1313.

[49] L. López-García, W. Cruz-Santos, A. García-Arellano, P. Filio-Aguilar, J. A. Cisneros-Martínez, R. Ramos-García, *Opt. Express* **2022**, *30*, 13714.

[50] W.-K. Yu, X.-F. Liu, X.-R. Yao, C. Wang, Y. Zhai, G.-J. Zhai, *Sci. Rep.* **2014**, *4*, 5834.

[51] Z. Zhang, X. Wang, G. Zheng, J. Zhong, *Opt. Express* **2017**, *25*, 19619.

[52] M.-J. Sun, L.-T. Meng, M. P. Edgar, M. J. Padgett, N. Radwell, *Sci. Rep.* **2017**, *7*, 3464.

[53] R. Dutta, S. Manzanera, A. Gambín-Regadera, E. Irles, E. Tajahuerce, J. Lancis, P. Artal, *Biomed. Opt. Express* **2019**, *10*, 4159.

[54] K. Zhang, W. Zuo, L. Zhang, *IEEE Trans. Image Process.* **2018**, *27*, 4608.

[55] M. Khorasaninejad, W. T. Chen, R. C. Devlin, J. Oh, A. Y. Zhu, F. Capasso, *Science* **2016**, *352*, 1190.

[56] S. Wang, P. C. Wu, V.-C. Su, Y.-C. Lai, M.-K. Chen, H. Y. Kuo, B. H. Chen, Y. H. Chen, T.-T. Huang, J.-H. Wang, R.-M. Lin, C.-H. Kuan, T. Li, Z. Wang, S. Zhu, D. P. Tsai, *Nat. Nanotechnol.* **2018**, *13*, 227.